The Valence-Detrapping Phase Transition in a Crystal of the Mixed-Valence Trinuclear Iron Cyanoacetate Complex $[Fe_3O(O_2CCH_2CN)_6(H_2O)_3]$

Tadahiro Nakamoto,*,†,[1a] Minoru Hanaya,[2] Motomi Katada,[1b] Kazutoyo Endo,[3] Susumu Kitagawa,[1a] and Hirotoshi Sano[4]

Department of Chemistry, Faculty of Science, Tokyo Metropolitan University, Minamiohsawa, Hachioji, Tokyo 192-03, Japan, Radioisotope Research Center, Tokyo Metropolitan University, Minamiohsawa, Hachioji, Tokyo 192-03, Japan, Department of Chemistry, Faculty of Science, Tokyo Institute of Technology, O-okayama 2, Meguro-ku, Tokyo 152, Japan, Showa College of Pharmaceutical Sciences, Higashi-tamagawagakuen, Machida, Tokyo 194, Japan, and Department of Environmental Science, School of Social Information Studies, Otsuma Women's University, Karakida, Tama, Tokyo 206, Japan

Received November 27, 1996[⊗]

A mixed-valence trinuclear iron cyanoacetate complex, $[Fe_3O(O_2CCH_2CN)_6(H_2O)_3]$ (**1**), was prepared, and the nature of the electron-detrapping phase transition was studied by a multitemperature single-crystal X-ray structure determination (296, 135, and 100 K) and calorimetry by comparison with an isostructural mixed-metal complex, $[CoFe_2O(O_2CCH_2CN)_6(H_2O)_3]$ (**2**). The mixed-valence states at various temperatures were also determined by ^{57}Fe Mössbauer spectroscopy. The Mössbauer spectrum of **1** showed a valence-detrapped state at room temperature. With decreasing temperature the spectrum was abruptly transformed into a valence-trapped state around 129 K, well corresponding to the heat-capacity anomaly due to the phase transition (T_{trs} = 128.2 K) observed in the calorimetry. The single-crystal X-ray structure determination revealed that **1** has an equilateral structure at 296 and 135 K, and that the structure changes into an isosceles one at 100 K due to the electron trapping. The crystal system of **1** at 296 K is rhombohedral, space group $R\bar{3}$ with $Z = 6$ and $a = 20.026(1)$ Å, $c = 12.292(2)$ Å; at 135 K, $a = 19.965(3)$ Å, $c = 12.145(4)$ Å; and at 100 K, the crystal system changes into triclinic system, space group $P\bar{1}$, with $Z = 2$ and $a = 12.094(2)$ Å, $b = 12.182(3)$ Å, $c = 12.208(3)$ Å, $\alpha = 110.04(2)°$, $\beta = 108.71(2)°$, $\gamma = 109.59(2)°$. The X-ray structure determination at 100 K suggests that the electronically trapped phase of **1** at low temperature is an antiferroelectrically ordered phase, because the distorted Fe_3O molecules, which are expected to possess a nonzero electronic dipole moment, oriented alternatively in the opposite direction with respect to the center of symmetry. On the other hand, no heat-capacity anomaly was observed in **2** between 7 and 300 K, and X-ray structure determination indicated that **2** shows no structure change when the temperature is decreased from 296 K down to 102 K. The crystal system of **2** at 296 K is rhombohedral, space group $R\bar{3}$ with $Z = 6$ and $a = 19.999(1)$ Å, $c = 12.259(1)$ Å; at 102 K, $a = 19.915(2)$ Å, $c = 12.061(1)$ Å. Even at 102 K the $CoFe_2O$ complex still has a C_3 axis, and the three metal ion sites are crystallographically equivalent because of a static positional disorder of two Fe^{III} ions and one Co^{II} ion. The activation energy of intramolecular electron transfer of **1** in the high-temperature disordered phase was estimated to be 3.99 kJ mol^{-1} from the temperature dependence of the Mössbauer spectra with the aid of the spectral simulation including the relaxation effect of intramolecular electron transfer. Finally the phase-transition mechanism of **1** was discussed in connection with the intermolecular dielectric interaction.

Introduction

Mixed-valence trinuclear iron carboxylate complexes, $[Fe^{III}_2Fe^{II}O(O_2CR)_6L_3]S$,[5] are one of the suitable systems for studying mixed-valence properties of discrete molecules in the solid state. These complexes enjoy the advantage of the use of ^{57}Fe Mössbauer spectroscopy, which provides information about the rate of intramolecular electron transfer. The first application of ^{57}Fe Mössbauer spectroscopy to the mixed-valence acetate complex $[Fe_3O(O_2CCH_3)_6(H_2O)_3]\cdot nH_2O$ found a temperature-dependent valence-detrapping process from the trapped-valence state at lower temperatures to the detrapped-valence state at room temperature.[6] The interpretation was that the rate of intramolecular electron transfer is less than the inherent time scale of ^{57}Fe Mössbauer spectroscopy ($\sim 10^7-10^8$ s^{-1}) at lower temperatures, and that it increases with increasing temperature and exceeds the ^{57}Fe Mössbauer time scale at room temperature.

In the last decade Hendrickson and co-workers have reported upon the valence-detrapping phase transition in mixed-valence acetate complexes $[Fe_3O(O_2CCH_3)_6L_3]S$[7,8] and mono-oxidized biferrocene derivatives.[9] They have shown that the valence-detrapping process occurs as an order−disorder phase transition, and that the rate of intramolecular electron transfer depends on the surrounding environment. In the case of mixed-valence Fe_3O complexes, the rate of intramolecular electron transfer is sensitively affected by the nature of the coordinated ligands, L, and/or solvate molecules, S. For instance, quite different temperature dependence of the mixed-valence state has been found in the crystalline phase even of the same Fe_3O molecule, depending on the presence or absence of the solvate molecules. Although the pyridine-solvated acetate complex $[Fe_3O(O_2CCH_3)_6(py)_3]py$ and the nonsolvated complex $[Fe_3O$-

† Present address: Advanced Science Research Center, Japan Atomic Energy Research Institute, Tokai-mura, Ibaraki 319-11, Japan.

⊗ Abstract published in *Advance ACS Abstracts,* September 1, 1997.

(1) (a) Department of Chemistry, Faculty of Science, Tokyo Metropolitan University. (b) Radioisotope Research Center, Tokyo Metropolitan University.

(2) Tokyo Institute of Technology.

(3) Showa College of Pharmaceutical Sciences.

(4) Otsuma Women's University.

(5) Cannon, R. D.; White, R. P. *Prog. Inorg. Chem.* **1988**, *36*, 195.

(6) Lupu, D.; Barb, D.; Filoti, G.; Morariu, M.; Tarina, D. *J. Inorg. Nucl. Chem.* **1972**, *34*, 2803.

S0020-1669(96)01438-3 CCC: $14.00

$(O_2CCH_3)_6(py)_3$] both show a valence-trapped state at lower temperatures in ^{57}Fe Mössbauer spectroscopy, the solvated complex becomes valence-detrapped at ~190 K whereas the nonsolvated complex remains in the valence-trapped state even at 315 K.[7a,c] The calorimetric study[8a] and ^{2}H-NMR study[7d] have demonstrated that the valence-detrapping process in the pyridine-solvated complex crystals occurs as an order−disorder phase transition accompanied by orientational disordering of the pyridine solvate molecules. The theoretical description for the valence-detrapping process given by Kambara et al.[10] based on the vibronic coupling model[11] has predicted that the phase transition due to the valence-detrapping process should occur at temperatures higher than room temperature for the nonsolvated complex crystals. Therefore, it has been concluded that the orientational disordering of the interstitial solvate molecules reduces the phase-transition temperature by assisting the intramolecular electron transfer. The interaction between the molecular dipole of the electron-localized Fe_3O complex and the permanent dipole of the solvate molecule has been considered to play an important role.[8,9,12] The other acetate complexes have also supported this proposal, and it has been generally considered that the solvate molecule is essential for the phase transition to occur below room temperature.

However, it has been found that some nonsolvated mixed-valence Fe_3O complexes, such as $[Fe_3O(O_2CC_{17}H_{35})_6(py)_3]$[13a] and $[Fe_3O(O_2CCMe_3)_6(Me_3CCO_2H)_3]$,[13f] which have long or bulky alkyl groups, also show a valence-detrapping phase transition below room temperature.[13] These results have indicated that the valence-detrapping phase transition is not always related to the presence of solvate molecules, and they suggest that the substituents of carboxylato ligands may play an important role in place of the solvate molecules.

On the other hand, a crystal-structure dependence of the rate of intramolecular electron transfer has been found in the nonsolvated phenyl acetate complex $[Fe_3O(O_2CCH_2Ph)_6(py)_3]$.[13h] ^{57}Fe Mössbauer spectra of the two different crystal forms of this complex show quite different temperature dependence; one shows a trapped-valence state at low temperature (8 K) but a detrapped-valence state at room temperature, whereas the other form shows a trapped-valence state even at room temperature. A similar crystal-structure dependence of the rate of intramolecular electron transfer has been found also in 1,1‴-di-*n*-butylbiferrocenium triiodide.[14] In this complex the crystal packing is quite different between the two forms; the crystal showing a detrapped-valence state has a higher symmetry in the structure of the 1,1‴-di-*n*-butylbiferrocenium monocation than the crystal showing a trapped-valence state. These facts indicate that the dynamic properties of the mixed-valence state depend on the whole crystal structure.

In this situation precise information on the difference between the trapped-valence phase and the detrapped-valence phase, especially in the crystal structure, of the same compound is indispensable in order to clarify the phenomenon of cooperative valence detrapping and to understand why the detrapped Fe_3O molecule changes into the trapped molecule when the temperature is lowered below room temperature. However, no structure determination of the trapped-valence phase converted from the detrapped phase has ever been reported. Furthermore, the previously reported valence-detrapping phase transitions of the mixed-valence Fe_3O complexes were always accompanied by the effects of the solvate molecules or the bulky carboxylate ligands, which bring undesirable complication to the extraction of the essential properties of the valence-detrapping phenomenon.

In a previous study, we reported the synthesis of $[Fe_3O(O_2CCH_2CN)_6(H_2O)_3]$, which shows very interesting characteristics.[15] The complex shows a temperature-dependent valence detrapping in its Mössbauer spectra accompanied by a phase transition in a rather low temperature region, ~130 K. Since this complex has a nonsolvated simple structure in contrast with the other previously reported complexes of the mixed-valence Fe_3O type, a detailed investigation of the valence-detrapping process and the associated phase transition will provide valuable information about the microscopic electronic structure of the valence-detrapped state, and also about the mechanisms of the process as well as those of the phase transition. In the present work, we used variable-temperature ^{57}Fe Mössbauer spectroscopy, adiabatic calorimetry, IR spectroscopy, and variable-temperature X-ray crystallography for this complex, and addressed the above issues on the basis of results which are free from the influence of the orientational disordering of solvate molecules and coordinated ligands. In addition, an isostructural mixed-metal complex, $[CoFe_2O(O_2CCH_2CN)_6(H_2O)_3]$ (**2**), which does not show valence detrapping, was also investigated with respect to its structural and thermal properties for the sake of comparison.

Experimental Section

Sample Preparation. $[Fe_3O(O_2CCH_2CN)_6(H_2O)_3]$ (1).[15] A solution of $NCCH_2CO_2H$ (4.3 g, 0.05 mol) and NaOH (2.0 g, 0.05 mol) in 30 mL of water was added to a solution of $FeCl_2 \cdot 4H_2O$ (5.0 g, 0.025 mol) in 20 mL of water. The mixture was allowed to stand in a shallow dish covered with a watch glass for a few weeks at room temperature. Dark red-brown needle-like crystals were filtered and washed with water and then acetone. The one-batch sample for heat capacity measurements was prepared on a scale 10 times as large as that described above by using a shallow tray (40 × 32 cm) instead of the dish.

(7) (a) Oh, S. M.; Hendrickson, D. N. *J. Am. Chem. Soc.* **1984**, *106*, 7984. (b) Oh, S. M.; Kambara, T.; Hendrickson, D. N. *J. Am. Chem. Soc.* **1985**, *107*, 5540. (c) Oh, S. M.; Hendrickson, D. N.; Hassett, K. L.; Raymond, E. D. *J. Am. Chem. Soc.* **1985**, *107*, 8009. (d) Woehler, S. E.; Wittebort, R. J.; Oh, S. M.; Hendrickson, D. N.; Inniss, D.; Strouse, C. E. *J. Am. Chem. Soc.* **1986**, *108*, 2938. (e) Woehler, S. E.; Wittebort, R. J.; Oh, S. M.; Kambara, T.; Hendrickson, D. N.; Inniss, D.; Strouse, C. E. *J. Am. Chem. Soc.* **1987**, *109*, 1063. (f) Oh, S. M.; Wilson, S. R.; Hendrickson, D. N.; Woehler, S. E.; Wittebort, R. J.; Inniss, D.; Strouse, C. E. *J. Am. Chem. Soc.* **1987**, *109*, 1073. (g) Jang, H. G.; Geib, S. J.; Kaneko, Y.; Nakano, M.; Sorai, M.; Rheingold, A. L.; Montez, B.; Hendrickson, D. N. *J. Am. Chem. Soc.* **1989**, *111*, 173. (h) Jang, H. G.; Kaji, K.; Sorai, M.; Wittebort, R. J.; Geib, S. J.; Rheingold, A. L.; Hendrickson, D. N. *Inorg. Chem.* **1990**, *29*, 3547. (i) Jang, H. G.; Wittebort, R. J.; Sorai, M.; Kaneko, Y.; Nakano, M.; Hendrickson, D. N. *Inorg. Chem.* **1992**, *31*, 2265.

(8) (a) Sorai, M.; Kaji, K.; Hendrickson, D. N.; Oh, S. M. *J. Am. Chem. Soc.* **1986**, *108*, 702. (b) Sorai, M.; Shiomi, Y.; Hendrickson, D. N.; Oh, S. M.; Kambara, T. *Inorg. Chem.* **1987**, *26*, 223. (c) Kaneko, Y.; Nakano, M.; Sorai, M.; Jang, H. G.; Hendrickson, D. N. *Inorg. Chem.* **1989**, *28*, 1067.

(9) Webb, R. J.; Hagen, P. M.; Wittebort, R. J.; Sorai, M.; Hendrickson, D. N. *Inorg. Chem.* **1992**, *31*, 1791 and references cited therein.

(10) Kambara, T.; Hendrickson, D. N.; Sorai, M.; Oh, S. M. *J. Chem. Phys.* **1986**, *85*, 2895.

(11) Wong, K. Y.; Schatz, P. N. *Prog. Inorg. Chem.* **1981**, *28*, 369.

(12) Sorai, M.; Hendrickson, D. N. *Pure Appl. Chem.* **1991**, *63*, 1503.

(13) (a) Nakamoto, T.; Katada, M.; Sano, H. *Chem. Lett.* **1990**, 225; **1991**, 1323. (b) Nakamoto, T.; Katada, M.; Sano, H. *Hyperfine Interactions* **1991**, *68*, 233. (c) Sato, T.; Nakamoto, T.; Katada, M.; Endo, K.; Sano, H. *Hyperfine Interactions* **1994**, *84*, 559. (d) Yoshida, M.; Nakamoto, T.; Kawata, S.; Katada, M.; Sano, H. *Hyperfine Interactions* **1994**, *84*, 583; 589. (e) Nakamoto, T.; Katada, M.; Kawata, S.; Kitagawa, S.; Sano, H.; Konno, M. *Hyperfine Interact.* **1994**, *93*, 1567. (f) Asamaki, K.; Nakamoto, T.; Kawata, S.; Katada, M.; Endo, K.; Sano, H. *Inorg. Chim. Acta* **1995**, *236*, 155. (g) Sato, T.; Ambe, F; Maeda, H.; Endo, K.; Katada, M.; Nakamoto, T.; Sano, H. *J. Am. Chem. Soc.* **1996**, *118*, 3450. (h) Nakamoto, T.; Yoshida, M.; Katada, M.; Kitagawa, S.; Endo, K.; Sano, H. *Polyhedron* **1996**, *15*, 2131.

(14) Nakashima, S. *Nucl. Instrum. Methods Phys. Res.* **1993**, *B76*, 408.

(15) Nakamoto, T.; Katada, M.; Kawata, S.; Kitagawa, S.; Kikuchi, K.; Ikemoto, I.; Endo, K.; Sano, H. *Chem. Lett.* **1993**, 1463.

Anal. Calcd for $C_{18}Fe_3H_{18}N_6O_{16}$: C, 29.14; H, 2.45; N, 11.33. Found: C, 29.39; H, 2.25; N, 11.23.

$[CoFe_2O(O_2CCH_2CN)_6(H_2O)_3]$ (2).[16] A solution of $CoCl_2 \cdot 6H_2O$ (23.8 g, 0.1 mol) in 50 mL of water was added to a solution of $NCCH_2CO_2H$ (17.2 g, 0.2 mol) and NaOH (8.0 g, 0.2 mol) in 30 mL of water, and then a solution of $FeCl_3 \cdot 6H_2O$ (2.7 g, 0.01 mol) in 20 mL of water was added to the preceding mixture. The resulting mixture was kept at rest for a few days at room temperature. Dark red-brown needle-like crystals were filtered and washed with water and then acetone. The one-batch sample for heat capacity measurements was prepared on a scale 10 times as large as that described above.

Anal. Calcd for $C_{18}CoFe_2H_{18}N_6O_{16}$: C, 29.01; Co, 7.91; Fe, 14.99; H, 2.44; N, 11.28. Found: C, 29.06; Co, 7.70; Fe, 15.08; H, 2.40; N, 11.22. The contents of Co and Fe were determined by neutron activation analysis.[17]

$[Fe_3O(O_2CCH_2CN)_6(H_2O)_3]NO_3 \cdot 5H_2O$ (3). The fully-oxidized iron cyanoacetate nitrate complex used for the IR spectroscopic study was prepared according to the method described for $[Fe_3O(O_2CCH_3)_6(H_2O)_3]NO_3 \cdot xH_2O$[18] with a modification. The details and crystal structure will be reported elsewhere.[19]

Anal. Calcd for $C_{18}Fe_3H_{28}N_7O_{24}$: C, 23.54; H, 2.67; N, 10.57. Found: C, 24.18; H, 3.16; N, 10.97.

Physical Measurements. ^{57}Fe Mössbauer Spectroscopy. Mössbauer spectra of the samples at various temperatures were measured against a ^{57}Co(Rh) source (925 MBq) moving in the constant acceleration mode at room temperature. Nonground samples were used even though the anisotropic effects could be emphasized, in order to avoid possible mechanochemical effects on the crystals. The crystalline samples were placed in a home-made acrylic cell to avoid exposure to a high-vacuum atmosphere. The spectra were fitted by least-squares fitting with Lorentzian lines. Velocity calibration was carried out by determining the magnetic splitting of natural iron foil. All of the isomer shift data were referred to metallic α-iron at room temperature.

Heat-Capacity Measurements. Heat-capacity measurements were performed in the temperature range between 14 and 300 K for **1** and between 7 and 300 K for **2** with a high-precision adiabatic calorimeter previously reported.[20] A Pt resistance thermometer and a Rh−Fe resistance thermometer were used for **1** and **2**, respectively, with calibration based on the ITS-90.[21] The imprecision and inaccuracy of the heat capacity were estimated to be less than ±0.06% and ±0.3%, respectively, from the results of the heat-capacity measurements for benzoic acid as a standard material.[20] The sample used for heat-capacity measurements was loaded in a calorimeter cell under an atmosphere of helium gas, and the cell was sealed vacuum-tight with indium wire. The samples for the measurements were obtained by the large-scale syntheses, and the mass of the sample used was 11.245 g (corresponding to 1.5154×10^{-2} mol) for **1** and 5.719 g (7.675×10^{-3} mol) for **2**.

The calorimeter cell loaded with the sample was placed under adiabatic conditions by keeping the adiabatic shield, surrounding the cell, always at the same temperature as the cell and by evacuating the space within the cryostat to 10^{-4} Pa. Heat-capacity measurements were carried out by an intermittent heating method,[22] and the spontaneous heat absorption associated with the enthalpy change of the sample due to a phase transition was monitored through observation of the spontaneous temperature drift rate of the calorimeter cell in the temperature-rating periods.

IR Measurements. IR spectra were recorded for a KBr pellet of the samples with a JASCO FT-IR-5MP spectrometer in the range 400−4300 cm^{-1} at room temperature. Variable-temperature IR measurements were performed for a KBr pellet of **1** in the range 400−4000 cm^{-1} by using a custom-made cryostat combined with an Iwatani Cryo-Techno Corporation Cryo-mini D230 compressor, and the spectra were recorded with a Perkin Elmer 1720X FT-IR spectrometer in the temperature range between 17 and 295 K.

X-ray Crystallographic Analysis. All measurements were made by using Mo *K*α (0.710 69 Å) radiation on an Enraf-Nonius CAD-4 κ-geometry diffractometer. Three standard reflections were remeasured to monitor the instrument and the crystal quality every 2 h. The intensities were corrected for Lorentz-polarization effects and for empirical absorption corrections based on a series of ψ scans. All of the crystal structures were solved by using a direct method program, SIR88.[23] All calculations were carried out with the computer software MolEN[24] on a Micro VAX 3400. In the low-temperature study, temperature was controlled by using a nitrogen gas-stream cryostat, Enraf-Nonius FR558SH. Temperature was determined by preliminary measurements under similar conditions using a calibrated K-type (chromel−alumel) thermocouple attached to a goniometer head on the diffractometer equipped with the cryostat. Temperature stability during the measurement at ∼100 K was determined to be ±0.5 K. To avoid shrinkage of the goniometer head and ice formation on the head, the head was lowered by mounting the crystal with a home-made long glass pin and a poor heat-conducting cover was put on the head. Before the intensity collection at low temperatures, preliminary diffraction studies were carried out at room temperature for the verification of the crystal quality.

The crystal-structure determination of **1** was carried out at 296, 135, and 100 K. The intensities were collected from two different crystals; one for 296 K and the other for 135 and 100 K. Crystallographic data are collected in Table 1. In the measurement at 296 K, a crystal with dimensions $0.30 \times 0.20 \times 0.20$ mm cut out from a longer needle-like crystal was mounted on the end of a glass fiber by epoxy cement. The unit cell parameters were obtained by a least-squares fit to the automatically centered settings of 25 reflections in the range $10° \le \theta \le 15°$. In the low-temperature study, the crystal with dimensions $0.60 \times 0.15 \times 0.10$ mm was mounted in a purchased glass capillary without any adhesive agent. The capillary was stuffed with quartz wool to avoid the crystal slipping during the data collection. In the measurement at 100 K, the unit cell parameters were obtained by a least-squares fit to the automatically centered settings of 22 reflections in the range $9° \le \theta \le 18°$. The intensity collection at 135 K was carried out for the same crystal subsequent to the data collection at 100 K. The unit cell parameters at 135 K were obtained by a least-squares fit to the automatically centered settings of 25 reflections in the range $10° \le \theta \le 19°$.

The crystal-structure determination of **2** was carried out at 296 and 102 K. The intensities were collected from two different crystals. Crystallographic data are collected in Table 2. In the measurement at 296 K, a crystal with dimensions $0.25 \times 0.25 \times 0.20$ mm cut out from a longer needle-like crystals was mounted on the end of a glass fiber by using epoxy cement. The unit cell parameters were obtained by a least-squares fit to the automatically centered settings of 21 reflections in the range $9° \le \theta \le 18°$. In the measurement at 102 K, a crystal with dimensions $0.15 \times 0.15 \times 0.15$ mm was mounted on the end of a glass fiber by using joint grease instead of epoxy cement. The unit cell parameters were obtained by a least-squares fit to the automatically centered settings of 17 reflections in the range $7° \le \theta \le 18°$.

Structure Analysis and Refinement.[25] **$[Fe_3O(O_2CCH_2CN)_6(H_2O)_3]$ (1).**[26] The structures of **1** at 296 and 135 K were solved in

(16) Sato, T.; Ambe, F. Private communication. This complex was prepared for use in a ^{57}Co emission Mössbauer spectroscopic study. For example: Sato, T.; Katada M.; Endo, K.; Nakada, M.; Sano, H. *J. Radioanal. Nucl. Chem.* **1993**, *173*, 107.

(17) Accurately weighed samples were sealed in a polyethylene sheet and irradiated for 24 h with a thermal neutron flux of 10^{11} n cm^{-2} s^{-1} under 100 kW operation at F-24 of the TRIGA II nuclear reactor at Atomic Energy Institute of Rikkyo University. Commercially purchased standard solutions of Fe and Co (1000 ppm, Wako) for atomic absorption photospectrometry were used as the references.

(18) Johnson, M. K.; Powell, D. B.; Cannon, R. D. *Spectrochim. Acta* **1981**, *37A*, 995.

(19) Nakamoto, T. Unpublished data. Crystal data: $[Fe_3O(O_2CCH_2CN)_6(H_2O)_3]NO_3 \cdot 5H_2O$, fw = 893.99, orthorhombic, space group *Pbca* (No. 61); $a = 15.166(1)$ Å, $b = 8.397(1)$ Å, $c = 25.391(1)$ Å, $V = 7084.6(6)$ Å^3; $Z = 8$; $d_{calc} = 1.676$ g cm^{-3}; $d_{obs} = 1.668$ g cm^{-3}; $\mu = 12.9$ cm^{-1}; $T = 296$ K; no. of reflections measured = 8963 total, 8196 unique, 4830 with $F_o^2 > 3\sigma(F_o^2)$; $5° < 2\theta < 55°$; Mo *K*α (0.710 73 Å); the present *R*, $R_w = 0.0503, 0.0732$; Fe···Fe = 3.325(1), 3.327(1), 3.328(1) Å.

(20) Fujimori, H.; Oguni, M. *J. Phys. Chem. Solids* **1993**, *54*, 271.

(21) Preston-Thomas, H. *Metrologia* **1990**, *27*, 3.

(22) Westerm, E. F., Jr.; Furukawa, G. T.; McCullough, J. P. In *Experimental Thermodynamics*; McCullough, J. P., Scott, D. W., Eds.; Butterworths: London, 1968; Vol. I, p 133.

(23) Burla, M. C.; Camalli, M.; Cascarano, G.; Giacovazzo, C.; Polidori, G.; Spagna, R.; Viterbo, D. *J. Appl. Crystallogr.* **1989**, *22*, 389.

(24) Enraf-Nonius, *MolEN. An Interactive Structure Solution Procedure*; Enraf-Nonius: Delft, The Netherlands, 1990.

Table 1. Crystallographic Data of $[Fe_3O(O_2CCH_2CN)_6(H_2O)_3]$ (**1**) at 296, 135, and 100 K

T, K	296	135	100
empirical formula	$C_{18}Fe_3H_{18}N_6O_{16}$	$C_{18}Fe_3H_{18}N_6O_{16}$	$C_{18}Fe_3H_{18}N_6O_{16}$
fw	741.91	741.91	741.91
cryst syst	trigonal	trigonal	triclinic
space group	$R\bar{3}$ (No. 148, rhombohedral axes)	$R\bar{3}$ (No. 148, rhombohedral axes)	$P\bar{1}$ (No. 2)
a, Å	12.261(2)	12.215(2)	12.094(2)[d]
b, Å			12.182(3)
c, Å			12.208(3)
α, deg	109.41(1)[c]	109.60(2)	110.04(2)
β, deg			108.71(2)
γ, deg			109.59(2)
V, Å^3	1423.0(1)	1397.2(8)	1385.7(8)
Z	2	2	2
D_{calcd}, g cm^{-3}	1.73	1.76	1.78
μ, cm^{-1}	15.9	16.2	16.3
radiation, Å	Mo Kα, 0.710 73	Mo Kα, 0.710 73	Mo Kα, 0.710 73
R[a]	0.0201	0.0305	0.0606
R_w[b]	0.0291	0.0449	0.0695
space group	$R\bar{3}$ (No. 148, hexagonal axes)	$R\bar{3}$ (No. 148, hexagonal axes)	
a, Å	20.026(1)	19.965(3)	
c, Å	12.292(2)	12.145(4)	
V, Å^3	4269.1(9)	4192(2)	
Z	6	6	

[a] $R = (\sum||F_o| - |F_c||)/(\sum|F_o|)$. [b] $R_w = [\sum w(|F_o| - |F_c|)^2/(\sum w|F_o|^2)]^{1/2}$. [c] See ref 25. [d] See ref 26.

the space group $R\bar{3}$ (No. 148, hexagonal setting) and refined by full-matrix least squares. Further cycles of refinement and difference Fourier maps located all hydrogen atoms. All non-hydrogen atoms were refined anisotropically while the hydrogen atoms were refined isotropically. The positional parameters and the isotropic thermal parameters of hydrogen atoms were refined freely. The final positional parameters for all atoms at 296 and 135 K are included in Tables S2 and S3, respectively (Supporting Information).

When the temperature was lowered to 100 K from 135 K, the reflection line width was found to be fairly broadened in the ω scans from ~0.6−1.0° to ~1.0−3.0°, suggesting a deterioration of the crystal quality when the crystal underwent the phase transition. However, no distinct splitting due to crystal twinning was found in the present measurement even for the higher θ reflections. At 100 K, as a consequence of the lower space symmetry, the number of unique observed reflections must be increased to ca. three times as great as that at 135 K. A total of 3508 reflections with $F_o^2 > 3\sigma(F_o^2)$, which corresponds to ~80% of expected reflections, were observed, while the other ~20% were discarded probably because originally weak reflections became weaker due to the reflections' broadening. The loss of the weak reflections did not affect the successful structure analysis. However, the experimental errors were slightly enlarged and the thermal parameters of the two carbon atoms were no longer representable by ellipsoids probably because of the deterioration of the crystal quality. A statistical study of the reflections shows that the symmetry center still exists although the 3-fold axis is lost, indicating that the actual space group is $P\bar{1}$ (No. 2) among the possible space groups, $P1$ (No. 1) and $P\bar{1}$ (No. 2). The structure was solved in the space group $P\bar{1}$ (No. 2), and all non-hydrogen atoms were refined anisotropically, but C(7) and C(16) atoms were refined isotropically. All of the hydrogen atoms were located from differential Fourier maps and refined isotropically under the constraint to move with the atom to which the hydrogen atom is bonded. The final positional parameters for all atoms at 100 K are included in Table S9 (Supporting Information).

(25) (a) Though all of the $R\bar{3}$ structures were solved by the hexagonal setting, the constants are shown with respect to the rhombohedral setting in Tables 1 and 2 for easy comparison. (b) The unit cell of each complex is a primitive rhombohedral with α = 109.41° and 109.45° at 296 K, which are very close to 109.47°, signifying a special case. In that case, the rhombohedral R cell can be transformed to a body-centered cubic cell (cubic I) with $a_c = (2/\sqrt{3})a_r$ as described in *International Tables for Crystallography* (Hahn, T., Ed.; Kluwer Academic Publishers: Dordrecht, 1992; 3rd revised ed., Vol. A, p 77). Indeed, a systematic search for the unit cell of the highest possible Laue symmetry using TRACER-II described by Lawton (Lawton, S. L. *J. Appl. Crystallogr.* **1973**, *6*, 309) was carried out for each complex, and the presence of a unit cell of higher Laue symmetry, cubic I, was indicated with a tolerance factor of 0.5. However, the Laue symmetry check for the cubic I cells indicated that even the lowest Laue symmetry of cubic system $m\bar{3}$ was not accepted. Consequently, the crystal systems of these complexes have been settled into rhombohedral, neither cubic nor tetragonal.

Table 2. Crystallographic Data of $[CoFe_2O(O_2CCH_2CN)_6(H_2O)_3]$ (**2**) at 296 and 102 K

T, K	296	102
empirical formula	$C_{18}CoFe_2H_{18}N_6O_{16}$	$C_{18}CoFe_2H_{18}N_6O_{16}$
fw	745.00	745.00
cryst syst	trigonal	trigonal
space group	$R\bar{3}$ (No. 148, rhombohedral axes)	$R\bar{3}$ (No. 148, rhombohedral axes)
a, Å	12.249(1)	12.181(1)
α, deg	109.45(1)[c]	109.67(1)
V, Å^3	1415.7(2)	1380.9(4)
Z	2	2
D_{calcd}, g cm^{-3}	1.75	1.79
μ, cm^{-1}	16.7	17.1
radiation, Å	Mo Kα, 0.710 73	Mo Kα, 0.710 73
2θ range, deg	5−55	5−52.6
unique data, $F_o^2 > 3\sigma(F_o^2)$	1492	1204
R[a]	0.0275	0.0305
R_w[b]	0.0345	0.0350
space group	$R\bar{3}$ (No. 148, hexagonal axes)	$R\bar{3}$ (No. 148, hexagonal axes)
a, Å	19.999(1)	19.915(2)
c, Å	12.259(1)	12.061(1)
V, Å^3	4246.3(5)	4143.6(8)
Z	6	6

[a] $R = (\sum||F_o| - |F_c||)/(1\sum|F_o|)$. [b] $R_w = [\sum w(|F_o| - |F_c|)^2/(\sum w|F_o|^2)]^{1/2}$. [c] See ref 25.

[$CoFe_2O(O_2CCH_2CN)_6(H_2O)_3$] (2). The structures of **2** at 296 and 102 K were solved similarly to the case of **1** at 296 and 135 K. The mixed FeCo site was refined as an Fe atom with a site-occupancy factor of $^2/_3$ and a Co atom with that of $^1/_3$ located on an identical coordinate, in which all positional parameters and thermal parameters were constrained to move together. The final positional parameters for all atoms at 296 and 102 K are included in Tables S16 and S17, respectively (Supporting Information).

(26) When the temperature is lowered from 135 to 100 K, at first sight the most important change appears as a shrinkage of the a axis by 0.121 Å from 12.215 Å (135 K) to 12.094 Å (100 K) whereas b and c axes show only smaller shrinkages of 0.033 and 0.007 Å, respectively, although those changes are caused by a different axis choice of unit cell at each temperature. In the triclinic crystal system, a unit cell must be chosen such that the a, b, and c axes are the shortest, whereas in the rhombohedral crystal system a unit cell must be chosen such that the 3-fold axis becomes a body-diagonal axis even if the 3-fold axis is shorter than the a axis. Owing to these agreements, the triclinic a axis at 100 K corresponds to the body-diagonal axis of the rhombohedral cell above 135 K in the present case. If the triclinic axes are transformed to correspond to the rhombohedral axes above 135 K by using a transformation matrix,

$$\begin{pmatrix} -1 & -1 & -1 \\ 0 & 1 & 0 \\ 0 & 0 & 1 \end{pmatrix}$$

the cell constants at 100 K are given as follows: $a' = 12.176(2)$ Å, $b' = 12.182(3)$ Å, $c' = 12.208(3)$ Å, $\alpha' = 110.04(2)°$, $\beta' = 109.95(2)°$, and $\gamma' = 108.90(2)°$. The constants with $a' \cong b' < c'$ and $\alpha' \cong \beta' > \gamma'$ within 3σ clearly indicate a slight but significant distortion from the rhombohedral cell.

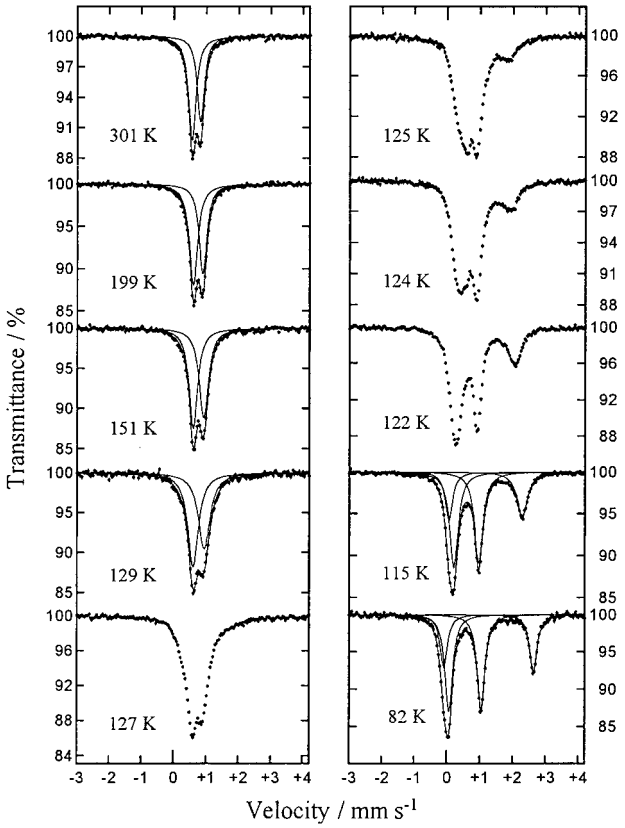

Figure 1. ^{57}Fe Mössbauer spectra of $[Fe_3O(O_2CCH_2CN)_6(H_2O)_3]$ (**1**).

Results

^{57}Fe Mössbauer Spectra. Mössbauer spectra of $[Fe_3O(O_2CCH_2CN)_6(H_2O)_3]$ (**1**) are shown in Figure 1,[27] and Mössbauer parameters are summarized in Table 3. At temperatures below 115 K two quadrupole-split doublets ascribed to a high-spin Fe^{II} and a high-spin Fe^{III} were observed with an area ratio of ∼1:2; from 122 K the spectra changed in their shape with increasing temperature; and then only one quadrupole-split doublet ascribed to an intermediate valence state between Fe^{II} and Fe^{III} was observed above 129 K. The asymmetric intensity of the quadrupole-split doublet is attributed to the preferential orientation of the needle crystals mounted on a sample holder. This temperature dependence of the Mössbauer spectra is considered to be due to the change in the rate of intramolecular electron transfer between Fe^{II} and Fe^{III} atoms in the Fe_3O moiety; the rate is slower than the Mössbauer time scale of $\sim 10^7 - 10^8$ s^{-1} below 115 K, increases to the time scale with increasing temperature between 122 and 127 K, and exceeds the time scale above 129 K.

In the Mössbauer spectra of intermediate valence state observed above 129 K, a notable difference was found between the averaging behavior of δ and ΔE_Q. The intermediate δ value was nearly equal to the estimated value by the weighted average of the δ values of Fe^{II} and Fe^{III}. On the other hand, the observed ΔE_Q value is very small compared with the value estimated by the weighted average of the ΔE_Q values of Fe^{II} and Fe^{III}. This unexpectedly small $\Delta E_{Q_{av}}$ value can only be explained by assuming that the $\Delta E_Q(Fe^{II})$ and $\Delta E_Q(Fe^{III})$ values have signs opposite to each other. This fact was taken into account in the relaxation model described later.

Mössbauer spectra of **2** are illustrated in Figure 2, and Mössbauer parameters are summarized in Table 3. The spectra show only one high-spin Fe^{III} doublet at all of the measured temperatures. The small temperature dependence of δ is attributable to the temperature dependence of the second-order Doppler shift.

Calorimetric Properties. Molar heat capacities obtained for **1** and **2** are plotted in Figure 3 with open circles and open squares, respectively.[28] As shown in this figure, **1** exhibited a heat-capacity anomaly due to a phase transition with a broad peak at around 130 K, while **2** exhibited no heat-capacity anomaly between 7 and 300 K. In Figure 4, the molar heat capacities of **1** in the phase transition temperature region and the spontaneous temperature drift rates of the calorimeter cell observed during the series of heat-capacity measurements are shown with circles and squares, respectively. The different symbols in this figure stand for the results obtained in the successive series of measurements. The heat capacities showed good agreement within the precision of the calorimeter among the series of measurements. The drift rates exhibited negative values, implying the existence of an endothermic effect, corresponding well to the heat-capacity anomaly in temperature. Although the heat-capacity anomaly has a broad shape without a sharp peak, the temperature dependence of the drift rates reveals the existence of the latent heat in the transition and suggests that the phase transition is of the first order. The phase-transition temperature in **1** was determined to be 128.2 ± 0.1 K from the temperature of the heat-capacity peak.

The facts that the temperature range of the phase transition in **1** corresponds well with the abrupt changes in Mössbauer spectra, from a superposition of doublets ascribed to high-spin Fe^{II} and Fe^{III} to only one doublet ascribed to an intermediate valence state between Fe^{II} and Fe^{III}, and that no heat-capacity anomaly was observed in **2**, which showed no anomalous temperature dependence in Mössbauer spectra, strongly suggest that the phase transition observed here is associated with the property change of the intramolecular electron transfer in the complex. Thus the transition corresponds to a change from the low-temperature ordered phase, in which the excess electron localizes on one of three Fe^{III} atoms in the Fe_3O moiety, to the higher-temperature disordered phase, in which the electron dynamically delocalizes over three Fe^{III} atoms.

In order to derive the anomalous part of the heat capacity due to the phase transition in **1**, the normal part of the heat capacity, i.e., the base line, in the phase transition temperature region was estimated from the heat-capacity data as a smooth curve. Unfortunately, no precise information about the intramolecular and molecular vibrations, which are usually used for the base-line estimation, was available for **1**. In this case, therefore, a fourth-order polynomial function[29] of temperature was employed to obtain an appropriate base line by fitting it to the heat-capacity data from 26 to 60 K and from 180 to 300 K, assuming that there is virtually no contribution to the heat capacity from the transition at such lower and higher temperature ranges than the phase-transition temperature. The solid line in Figure 5 represents the estimated base line for the observed heat capacities represented by open circles, and open squares stand for the anomalous part of the heat capacity of **1** due to the phase transition obtained by subtracting the base line from the observed heat capacities. The transition enthalpy, $\Delta_{trs}H_m$, and the transition entropy, $\Delta_{trs}S_m$, were calculated from the anomalous part by integrating it with respect to T and ln T, and they were evaluated to be 1003 J mol^{-1} and 9.06 J K^{-1} mol^{-1}, respectively.

(27) These spectra were obtained from the samples used in the heat-capacity measurement, and they are very slightly different from those previously presented in ref 15.

(28) Tabulated heat-capacity data of these complexes are available as Supporting Information.

(29) $C_{p,m}(T) = -71.99 + 5.996T - (1.934 \times 10^{-2})T^2 + (4.273 \times 10^{-5})T^3 - (3.890 \times 10^{-8})T^4$.

Table 3. Mössbauer Parameters of $[Fe_3O(O_2CCH_2CN)_6(H_2O)_3]$ (**1**) and $[CoFe_2O(O_2CCH_2CN)_6(H_2O_3]$ (**2**)

	δ,[a] mm s^{-1}			ΔE_Q, mm s^{-1}			Γ,[b] mm s^{-1}			area, %		
T, K	Fe^{II}	Fe^{av}	Fe^{III}	Fe^{II}	Fe^{av}	Fe^{III}	Fe^{II}	Fe^{av}	Fe^{III}	Fe^{II}	Fe^{av}	Fe^{III}
					$[Fe_3O(O_2CCH_2CN)_6(H_2O_3]$ (**1**)							
301		0.680(1)			0.258(3)			0.270(5) 0.259(6)			100	
248		0.707(2)			0.271(4)			0.279(8) 0.275(9)			100	
199		0.738(1)			0.290(3)			0.300(5) 0.283(6)			100	
151		0.756(2)			0.320(3)			0.307(6) 0.340(8)			100	
129		0.760(3)			0.336(7)			0.357(11) 0.453(14)			100	
104	1.234(5)		0.568(3)	2.507(11)		0.884(6)	0.258(7) 0.308(11)		0.289(5)	35(2)		65(2)
82	1.274(3)		0.554(2)	2.727(7)		0.979(4)	0.258(7)		0.275(4)	35(1)		65(1)
					$[CoFe_2O(O_2CCH_2CN)_6(H_2O_3]$ (**2**)							
299			0.434(1)			1.058(3)			0.256(5) 0.268(7)			100
184			0.496(2)			1.084(4)			0.275(8) 0.273(10)			100
80			0.546(2)			1.112(3)			0.271(7) 0.278(8)			100

[a] All of the isomer shift data are referred to metallic α-iron at room temperature. [b] Two values of Γ are indicated for an asymmetric quadrupole-split doublet and listed in order of increasing velocity of the peak.

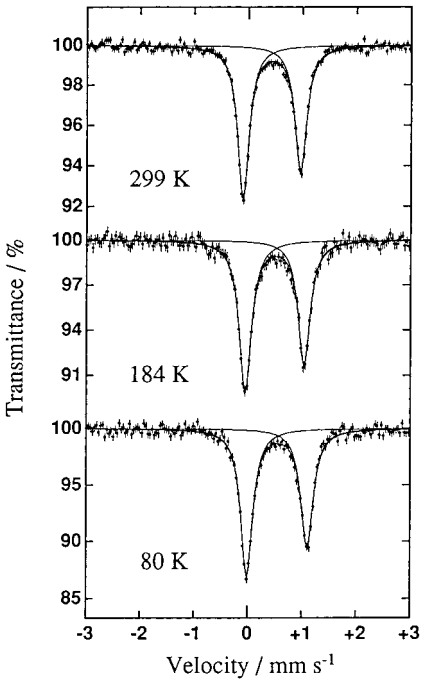

Figure 2. ^{57}Fe Mössbauer spectra of $[CoFe_2O(O_2CCH_2CN)_6(H_2O)_3]$ (**2**).

Figure 6 represents the temperature evolution of the excess entropy of **1**, showing that the disordering begins at temperatures rather lower than the transition temperature of 128.2 K.

X-ray Structure Analyses. An ORTEP[30] drawing of the molecular structure of **1** at 296 K is shown in Figure 7 with that at 135 K, and bond angles and distances are summarized in Tables 4 and 5. The structure of **1** at 296 K shows a typical triangular unit: three iron atoms with a triply bridged oxygen atom at a center, six bridged carboxylate ligands, and three coordinated H_2O ligands. The central oxygen atom is placed in the Fe_3 plane within twice the estimated standard deviation (0.0045(23) Å) and located on a crystallographic 3-fold symmetry axis. Therefore, the three Fe atoms are crystallographically equivalent with dynamic disorder due to the mobile electron. The detailed structure description for the molecular structure and the intermolecular hydrogen bonds have been reported previously in our preliminary publication.[15]

(30) Johnson, C. K. ORTEP. Report ORNL-3794; Oak Ridge National Laboratory: Oak Ridge, TN, 1965.

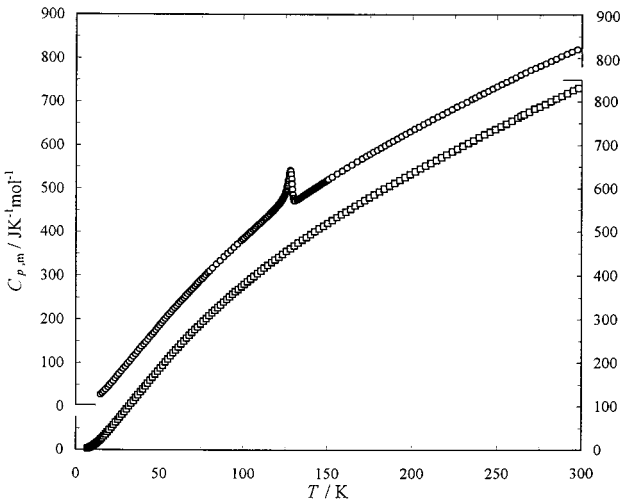

Figure 3. Molar heat capacities of trinuclear mixed-valence complexes: ○, $[Fe_3O(O_2CCH_2CN)_6(H_2O)_3]$ (**1**); □, $[CoFe_2O(O_2CCH_2CN)_6(H_2O)_3]$ (**2**).

When the temperature was lowered from 296 to 135 K, no significant dimensional change or symmetrical change was found in the structure of **1**. The three Fe atoms are still crystallographically equivalent at 135 K, although the distance between Fe and the central O showed a slight shrinkage from 1.8951(3) to 1.8924(5) Å probably because of a common thermal property due to anharmonic potential surface for interatomic bonds, namely, negative thermal expansion. The other intramolecular bond distances showed no significant ($>3\sigma$) changes with decreasing temperature because of the counterbalance between the shrinkage by the negative thermal expansion and the effective expansion by the decrease of the amplitude of rigid body motion.[31]

When the temperature was further lowered to 100 K, a significant change occurred in the crystal structure of **1**, although

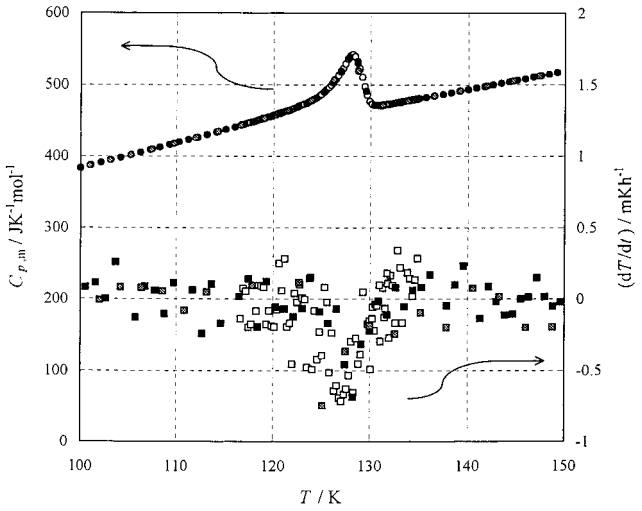

Figure 4. Molar heat capacity of $[Fe_3O(O_2CCH_2CN)_6(H_2O)_3]$ (**1**) in the phase transition temperature region (○) and spontaneous temperature drift rates observed during the series of heat-capacity measurements (□). The different symbols stand for the results obtained in the successive series of measurements.

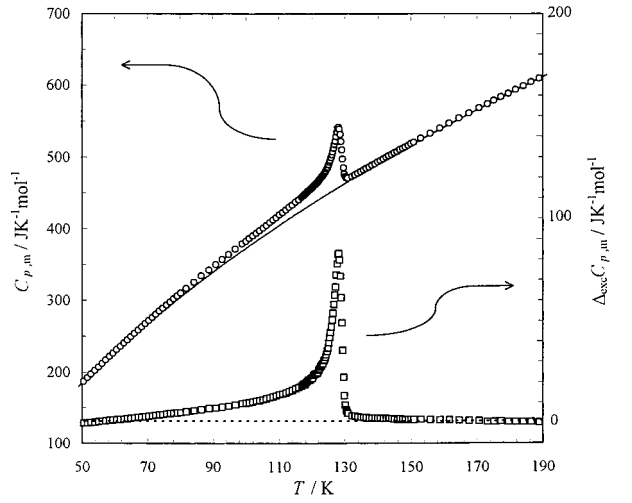

Figure 5. Molar heat capacity of $[Fe_3O(O_2CCH_2CN)_6(H_2O)_3]$ (**1**) (○) and excess heat capacity due to the phase transition (□). The solid line indicates the estimated normal heat-capacity curve from the heat-capacity data in 26−60 and 180−300 K with a fourth-order polynomial function of temperature.

there was no appreciable dimensional change in the intermolecular hydrogen bonds. An ORTEP drawing of the molecular structure of **1** at 100 K is shown in Figure 8, and selected bond distances (Å) and angles (deg) are summarized in Tables 6 and 7. The main structural change is that the space group became $P\bar{1}$, in which the Fe_3 triangle loses the 3-fold axis and becomes an isosceles triangle with Fe(1)−Fe(2) = 3.282(1) Å, Fe(1)−Fe(3) = 3.280(1) Å, and Fe(2)−Fe(3) = 3.258(2) Å. The structural change is also seen through the dimensional changes of the Fe−ligand distances. One of the three Fe−(μ_3-O) distances becomes longer and the other two become shorter than that at 135 K; Fe(1)−O = 1.953(4) Å, Fe(2)−O = 1.859(4) Å, and Fe(3)−O = 1.859(6) Å, which are consistent with the typical values for Fe^{II} and Fe^{III}.[5] The presence of one longer and two shorter Fe−(μ_3-O) distances strongly suggests that the Fe(1) atom is Fe^{II} and the Fe(2) and Fe(3) are Fe^{III}, and that the structural change is clearly caused by the electron trapping. This deviation from equilateral structure is much larger than

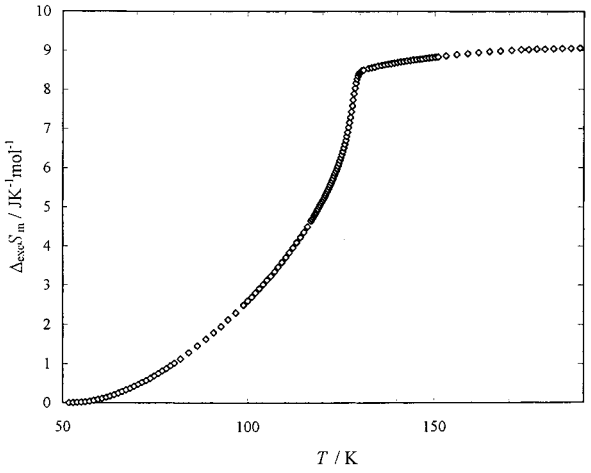

Figure 6. Temperature evolution of the excess entropy of $[Fe_3O(O_2CCH_2CN)_6(H_2O)_3]$ (**1**).

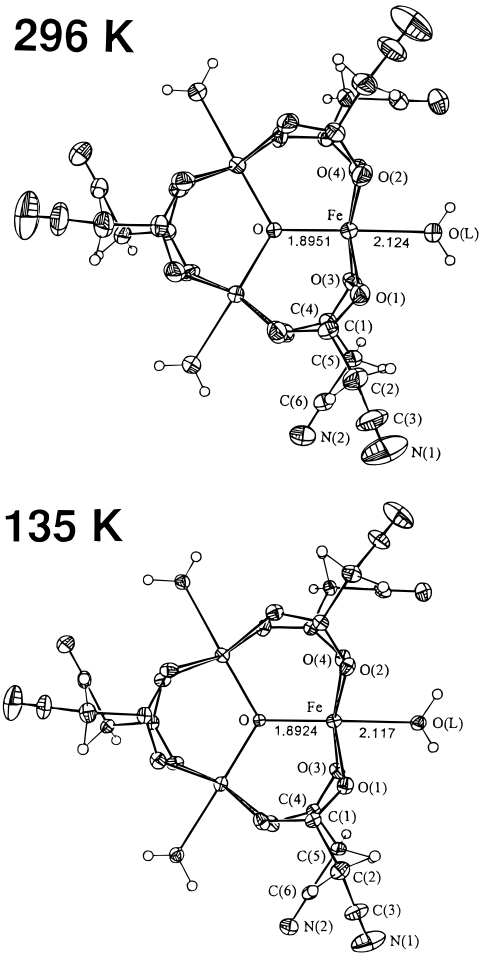

Figure 7. Comparison of the molecular structures of $[Fe_3O(O_2CCH_2CN)_6(H_2O)_3]$ (**1**) at 296 and 135 K. The thermal ellipsoids are drawn at the 50% probability level.

that predicted by the scalene model[32] based on the magnetic Jahn−Teller effect, implying that the magnetic effects on the molecular structure are negligible in the present case.

Another important feature in this structure is that the inversion center still remains between every pair of adjacent molecules although the 3-fold axis has been lost, indicating that the

(31) Ogawa, K.; Sano, T.; Yoshimura, S.; Takeuchi, Y.; Toriumi, K. *J. Am. Chem. Soc.* **1992,** *114*, 1041.

(32) Cannon, R. D.; Jayasooriya, U. A.; Wu, R.; arapKoske, S. K.; Stride, J. A.; Nielsen, O. F.; White, R. P.; Kearley, G. J.; Summerfield, D. *J. Am. Chem. Soc.* **1994**, *116*, 11869.

Table 4. Selected Bond Lengths (Å) for $[Fe_3O(O_2CCH_2CN)_6(H_2O)_3]$ (**1**) at 296 and 135 K

	296 K	135 K		296 K	135 K
Fe−O	1.8951(3)	1.8924(5)	C(1)−C(2)	1.522(3)	1.527(4)
Fe−O(L)	2.124(2)	2.117(2)	C(2)−C(3)	1.446(3)	1.469(5)
Fe−O(1)	2.067(1)	2.067(2)	C(3)−N(1)	1.119(4)	1.124(5)
Fe−O(2)	2.062(1)	2.067(2)	O(3)−C(4)	1.248(3)	1.256(2)
Fe−O(3)	2.055(1)	2.060(2)	O(4)−C(4)	1.249(3)	1.257(4)
Fe−O(4)	2.071(1)	2.074(2)	C(4)−C(5)	1.518(2)	1.521(4)
O(1)−C(1)	1.245(3)	1.248(3)	C(5)−C(6)	1.455(3)	1.456(3)
O(2)−C(1)	1.249(3)	1.259(4)	C(6)−N(2)	1.128(2)	1.138(3)

Table 5. Selected Bond Angles (deg) for $[Fe_3O(O_2CCH_2CN)_6(H_2O)_3]$ (**1**) at 296 and 135 K

	296 K	135 K
O−Fe−O(L)	178.59(5)	178.41(8)
O−Fe−O(1)	96.25(6)	96.29(9)
O−Fe−O(2)	96.23(7)	96.3(1)
O−Fe−O(3)	95.42(7)	95.3(1)
O−Fe−O(4)	97.62(6)	97.50(9)
Fe−O(1)−C(1)	133.2(1)	133.5(2)
Fe−O(2)−C(1)	127.3(1)	125.4(2)
Fe−O(3)−C(4)	127.7(1)	126.2(2)
Fe−O(4)−C(4)	131.1(1)	131.4(2)
O(1)−C(1)−O(2)	126.8(2)	127.1(3)
O(1)−C(1)−C(2)	116.4(2)	116.6(3)
O(2)−C(1)−C(2)	116.7(2)	116.3(2)
C(1)−C(2)−C(3)	110.2(2)	109.5(3)
C(2)−C(3)−N(1)	178.7(3)	178.6(4)
O(3)−C(4)−O(4)	127.3(2)	127.1(3)
O(3)−C(4)−C(5)	114.6(2)	114.6(3)
O(4)−C(4)−C(5)	118.0(2)	118.3(2)
C(4)−C(5)−C(6)	115.1(2)	114.6(3)
C(5)−C(6)−N(2)	178.1(3)	178.0(4)

isosceles Fe_3O moieties are alternatively oriented in the opposite direction in the crystal.

Figure 9 shows the molecular structures of **2** at 296 and 102 K, and bond distances and bond angles are summarized in Tables 8 and 9. Although **2** was revealed to be isostructural to **1** at 296 K, **2** did not change crystal system and space group even when cooled down to 102 K, keeping the 3-fold axis at the central O atom at 102 K. The three metal ion sites are crystallographically equivalent because of a static disorder of the positions of one Co^{II} ion and two Fe^{III} ions. The metal−(μ_3-O) distance, 1.8933(5) Å at 296 K, is slightly shorter than that of **1** because of the smaller ionic radius of high-spin Co^{II} (0.885 Å) than that of high-spin Fe^{II} (0.920 Å),[33] and corresponding to that the unit cell volume of **2** is smaller than that of **1**.

Infrared Spectroscopy. Infrared spectra observed for KBr pellets at room temperature of **1**, **2**, and the fully oxidized iron complex $[Fe^{III}_3O(O_2CCH_2CN)_6(H_2O)_3]NO_3{\cdot}5H_2O$ (**3**) are shown in Figure 10. In the $\nu_{as}(M_3O)$ region (∼550−720 cm^{-1}), appreciable differences are also observed among the three complexes. According to the description by Cannon and coworkers,[34] a shaded band at 586.4 cm^{-1} shown in the spectrum of **3** was assigned to the $\nu_{as}(Fe^{III}_3O)$ band. This band splits into two bands marked with asterisks (*) at 555.5 and 704.1 cm^{-1} in **2** and at 551.7 and 698.3 cm^{-1} in **1**, respectively. In the mixed-valence complex, the reduction in site symmetry from D_{3h} to C_{2v} has been found to cause a degeneracy of the ν_{as}-(M_3O) mode, and two bands are observed at ∼550 and 720 cm^{-1}. As shown in Figure 11, these two bands of **1** are observed more clearly when the temperature is lowered to 17 K, although lowering the temperature induced some modifications in the spectrum. Similar splittings observed for both **1** and **2** have

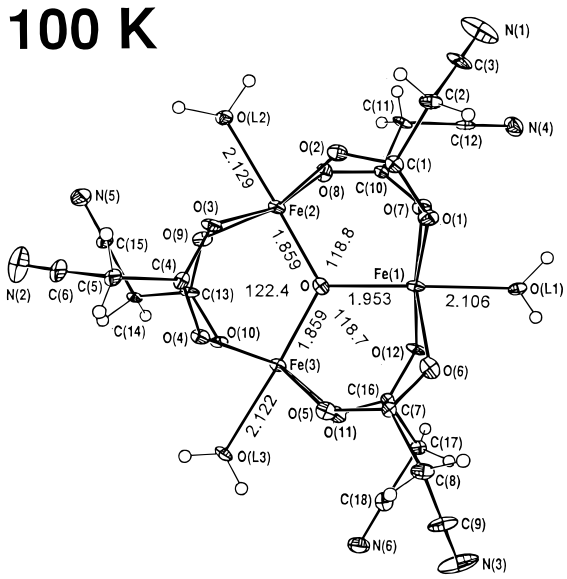

Figure 8. Molecular structure of $[Fe_3O(O_2CCH_2CN)_6(H_2O)_3]$ (**1**) at 100 K. The thermal ellipsoids are drawn at the 50% probability level.

Table 6. Selected Bond Lengths (Å) for $[Fe_3O(O_2CCH_2CN)_6(H_2O)_3]$ (**1**) at 100 K

Fe(1)−O	1.953(4)	Fe(2)−O	1.859(4)	Fe(3)−O	1.859(6)
Fe(1)−O(L1)	2.106(4)	Fe(2)−O(L2)	2.129(4)	Fe(3)−O(L3)	2.122(6)
Fe(1)−O(1)	2.093(6)	Fe(2)−O(3)	2.064(6)	Fe(3)−O(5)	2.021(4)
Fe(1)−O(6)	2.102(5)	Fe(2)−O(2)	2.021(4)	Fe(3)−O(4)	2.056(5)
Fe(1)−O(7)	2.118(6)	Fe(2)−O(9)	2.074(4)	Fe(3)−O(11)	2.035(5)
Fe(1)−O(12)	2.098(6)	Fe(2)−O(8)	2.038(6)	Fe(3)−O(10)	2.041(4)
O(1)−C(1)	1.249(8)	O(3)−C(4)	1.25(1)	O(5)−C(7)	1.260(6)
O(2)−C(1)	1.245(5)	O(4)−C(4)	1.251(9)	O(6)−C(7)	1.25(1)
C(1)−C(2)	1.53(1)	C(4)−C(5)	1.52(1)	C(7)−C(8)	1.534(9)
C(2)−C(3)	1.46(1)	C(5)−C(6)	1.452(7)	C(8)−C(9)	1.45(1)
C(3)−N(1)	1.13(1)	C(6)−N(2)	1.132(8)	C(9)−N(3)	1.14(1)
O(7)−C(10)	1.251(6)	O(9)−C(13)	1.26(1)	O(11)−C(16)	1.251(9)
O(8)−C(10)	1.252(7)	O(10)−C(13)	1.255(7)	O(12)−C(16)	1.26(1)
C(10)−C(11)	1.52(1)	C(13)−C(14)	1.501(7)	C(16)−C(17)	1.50(1)
C(11)−C(12)	1.444(8)	C(14)−C(15)	1.446(9)	C(17)−C(18)	1.45(1)
C(12)−N(4)	1.136(8)	C(15)−N(5)	1.144(8)	C(18)−N(6)	1.15(1)

indicated the C_{2v} site symmetry in both M_3O centers, i.e., the excess electron in **1** is trapped on one of the three Fe^{III} ions on the IR time scale (∼10^{12}−10^{13} s^{-1}) at any temperature below room temperature.

Discussion

Microscopic States in an Electronically Disordered Phase. From the beginning of the study on intramolecular electron transfer in mixed-valence Fe_3O complexes, it has been recognized that there is more or less a contribution of static *delocalization*.[6,35,36] The contribution of static delocalization

(33) Shannon, R. D. *Acta Crystallogr.* **1976**, *A32*, 751.

(34) Johnson, M. K.; Cannon, R. D.; Powell, D. B. *Spectrochim. Acta* **1982**, *38A*, 307. Cannon, R. D.; Montri, L.; Brown, D. B.; Marshall, K. M.; Elliott, C. M. *J. Am. Chem. Soc.* **1984**, *106*, 2591. Montri, L.; Cannon, R. D. *Spectrochim. Acta* **1985**, *41A*, 643. Meesuk, L.; Jayasooriya, U. A.; Cannon, R. D. *J. Am. Chem. Soc.* **1987**, *109*, 2009. Meesuk, L.; Jayasooriya, U. A.; Cannon, R. D. *Spectrochim. Acta* **1987**, *43A*, 687. Meesuk, L.; White, R. P.; Templeton, B.; Jayasooriya, U. A.; Cannon, R. D. *Inorg. Chem.* **1990**, *29*, 2389. White, R. P.; Wilson, L. M.; Williamson, D. J.; Moore, G. R.; Jayasooriya, U. A.; Cannon, R. D. *Spectrochim. Acta* **1990**, *46A*, 917. Anson, C. E.; Chai-Sa'ard, N.; Bourke, J. P.; Cannon, R. D.; Jayasooriya, U. A.; Powell, A. K. *Inorg. Chem.* **1993**, *32*, 1502. Cannon, R. D.; Jayasooriya, U. A.; Montri, L.; Saad, A. K.; Karu, E.; Bollen, S. K.; Sanderson, W. R.; Powell, A. K.; Blake, A. B. *J. Chem. Soc., Dalton Trans.* **1993**, 2005. Ohto, A.; Tokiwa-Yamamoto, A.; Abe, M.; Ito, T.; Sasaki, Y.; Umakoshi, K.; Cannon, R. D. *Chem. Lett.* **1995**, 97. References 18 and 31.

(35) Gol'danskii, V. I.; Alekseev, V. P.; Stukan, R. A.; Turta, K. I.; Ablov, A. V. *Dokl. Akad. Nauk SSSR* **1973**, *213*, 867; *Dokl. Phys. Chem.* **1973**, *213*, 1063.

Table 7. Selected Bond Angles (deg) for $[Fe_3O(O_2CCH_2CN)_6(H_2O)_3]$ (**1**) at 100 K

O−Fe(1)−O(L1)	177.7(2)	O−Fe(2)−O(L2)	178.0(2)	O−Fe(3)−O(L3)	176.5(1)
O−Fe(1)−O(1)	94.8(2)	O−Fe(2)−O(2)	98.5(2)	O−Fe(3)−O(4)	96.2(2)
O−Fe(1)−O(6)	95.6(2)	O−Fe(2)−O(3)	96.1(2)	O−Fe(3)−O(5)	99.0(2)
O−Fe(1)−O(7)	95.8(2)	O−Fe(2)−O(8)	96.9(2)	O−Fe(3)−O(10)	94.9(2)
O−Fe(1)−O(12)	92.6(2)	O−Fe(2)−O(9)	92.6(2)	O−Fe(3)−O(11)	99.2(2)
Fe(1)−O(1)−C(1)	124.5(4)	Fe(2)−O(3)−C(4)	126.0(5)	Fe(3)−O(5)−C(7)	125.0(5)
Fe(1)−O(7)−C(10)	131.4(5)	Fe(2)−O(9)−C(13)	131.7(3)	Fe(3)−O(11)−C(16)	131.5(5)
Fe(1)−O(6)−C(7)	132.5(3)	Fe(2)−O(2)−C(1)	133.2(5)	Fe(3)−O(4)−C(4)	133.6(5)
Fe(1)−O(12)−C(16)	125.7(5)	Fe(2)−O(8)−C(10)	125.8(4)	Fe(3)−O(10)−C(13)	126.4(5)
O(1)−C(1)−O(2)	127.9(7)	O(3)−C(4)−O(4)	126.2(7)	O(5)−C(7)−O(6)	128.1(6)
O(1)−C(1)−C(2)	116.2(4)	O(3)−C(4)−C(5)	116.5(6)	O(5)−C(7)−C(8)	116.4(7)
O(2)−C(1)−C(2)	115.8(6)	O(4)−C(4)−C(5)	117.3(7)	O(6)−C(7)−C(8)	115.3(4)
C(1)−C(2)−C(3)	109.3(7)	C(4)−C(5)−C(6)	108.9(7)	C(7)−C(8)−C(9)	110.8(7)
C(2)−C(3)−N(1)	179.1(5)	C(5)−C(6)−N(2)	179(1)	C(8)−C(9)−N(3)	178(1)
O(7)−C(10)−O(8)	127.6(7)	O(9)−C(13)−O(10)	126.4(5)	O(11)−C(16)−O(12)	126.7(7)
O(7)−C(10)−C(11)	117.7(5)	O(9)−C(13)−C(14)	118.1(5)	O(11)−C(16)−C(17)	118.3(7)
O(8)−C(10)−C(11)	114.7(5)	O(10)−C(13)−C(14)	115.5(7)	O(12)−C(16)−C(17)	114.8(6)
C(10)−C(11)−C(12)	115.4(5)	C(13)−C(14)−C(15)	115.6(7)	C(16)−C(17)−C(18)	115.2(6)
C(11)−C(12)−N(4)	179.1(7)	C(14)−C(15)−N(5)	179.5(7)	C(17)−C(18)−N(6)	177.9(7)
Fe(2)−O−Fe(3)	122.4(2)	Fe(1)−O−Fe(3)	118.7(2)	Fe(1)−O−Fe(2)	118.8(3)
Fe(2)−Fe(1)−Fe(3)	59.55(3)	Fe(1)−Fe(2)−Fe(3)	60.20(3)	Fe(1)−Fe(3)−Fe(2)	60.25(3)

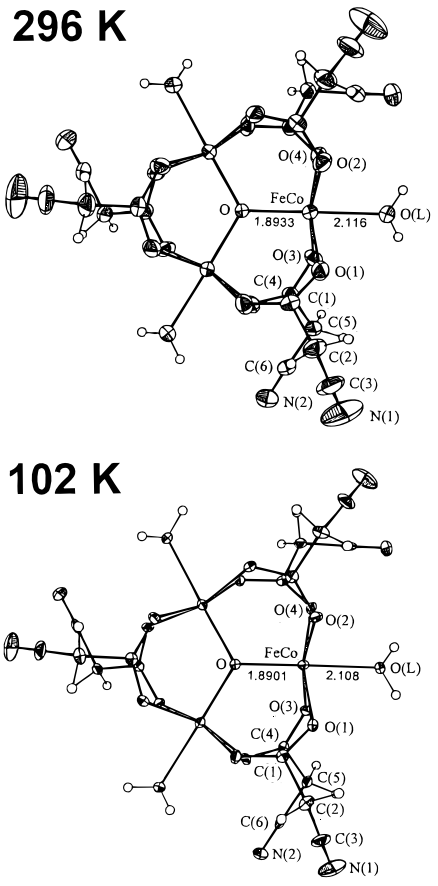

Figure 9. Comparison of the molecular structures of $[CoFe_2O(O_2CCH_2CN)_6(H_2O)_3]$ (**2**) at 296 and 102 K. The thermal ellipsoids are drawn at the 50% probability level.

depends on the shape of the vibronic potential well and affects the interpretation of the experimental results. However, there is no valid method to confirm the existence of the statically delocalized state in a dynamically detrapped phase except heat-capacity measurement. On the basis of a vibronic model,[11] Kambara et al.[10] have shown a possible quadruple-well-shaped potential diagram in a certain case besides a single-well- or a triple-well-shaped diagram of potential energy in mixed-valence Fe_3O complexes. If an Fe_3O complex has a quadruple-well-shaped potential, the contribution of electron detrapping to the transition entropy will be $R \ln 4$ rather than $R \ln 3$.[12] However, the obtained value of the transition entropy for **1**, 9.06 J K^{-1} mol^{-1}, is quite close to $R \ln 3$ (=9.13 J K^{-1} mol^{-1}), which strongly supports a triple-well-shaped potential energy surface in the disordered room-temperature phase, implying no contribution of static *delocalization* in the present case.

In Figure 12, possible phases in the crystal of the present complexes are illustrated in a similar way to Kambara's theoretical description.[10] Since X-ray crystallography can determine only a time-averaged and/or a space-averaged structure even if there are several microstructures regardless of dynamic or static, both **1** and **2** seem to have an equilateral triangular structure at room temperature as if their states correspond to a statically *delocalized* state described as phase

Table 8. Selected Bond Lengths (Å) for $[CoFe_2O(O_2CCH_2CN)_6(H_2O)_3]$ (**2**) at 296 and 102 K

	296 K	102 K		296 K	102 K
FeCo−O	1.8933(5)	1.8901(8)	C(1)−C(2)	1.526(3)	1.534(5)
FeCo−O(L)	2.116(2)	2.108(3)	C(2)−C(3)	1.450(4)	1.461(5)
FeCo−O(1)	2.059(2)	2.060(2)	C(3)−N(1)	1.121(5)	1.134(5)
FeCo−O(2)	2.058(2)	2.050(2)	O(3)−C(4)	1.253(3)	1.259(3)
FeCo−O(3)	2.042(2)	2.040(2)	O(4)−C(4)	1.245(3)	1.248(4)
FeCo−O(4)	2.062(2)	2.065(2)	C(4)−C(5)	1.524(3)	1.528(5)
O(1)−C(1)	1.245(4)	1.254(3)	C(5)−C(6)	1.450(4)	1.464(4)
O(2)−C(1)	1.245(3)	1.255(5)	C(6)−N(2)	1.128(4)	1.143(3)

Table 9. Selected Bond Angles (deg) for $[CoFe_2O(O_2CCH_2CN)_6(H_2O)_3]$ (**2**) at 296 and 102 K

	296 K	102 K
O−FeCo−O(L)	178.83(7)	178.3(1)
O−FeCo−O(1)	96.14(8)	96.3(1)
O−FeCo−O(2)	95.93(9)	96.2(1)
O−FeCo−O(3)	95.52(9)	95.3(1)
O−FeCo−O(4)	97.53(8)	97.4(1)
FeCo−O(1)−C(1)	133.2(2)	132.7(3)
FeCo−O(2)−C(1)	126.7(2)	125.0(2)
FeCo−O(3)−C(4)	127.2(2)	125.7(2)
FeCo−O(4)−C(4)	131.4(2)	131.3(2)
O(1)−C(1)−O(2)	127.0(2)	127.8(3)
O(1)−C(1)−C(2)	116.4(2)	115.9(3)
O(2)−C(1)−C(2)	116.6(3)	116.3(3)
C(1)−C(2)−C(3)	109.4(2)	108.7(3)
C(2)−C(3)−N(1)	180(1)	179.5(4)
O(3)−C(4)−O(4)	127.4(2)	127.6(3)
O(3)−C(4)−C(5)	114.5(2)	114.0(3)
O(4)−C(4)−C(5)	118.1(2)	118.4(2)
C(4)−C(5)−C(6)	114.7(2)	114.2(3)
C(5)−C(6)−N(2)	177.8(3)	178.5(4)

(36) Dziobkowski, C. T.; Wrobleski, J. T.; Brown, D. B. *Inorg. Chem.* **1981**, *20*, 679.

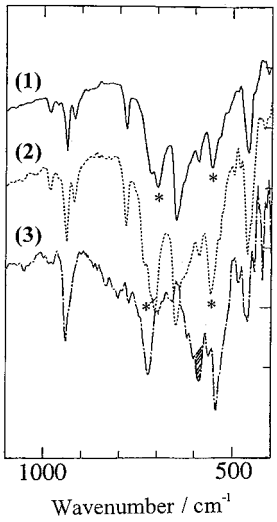

Figure 10. FT-IR spectra of KBr pellets of $[Fe_3O(O_2CCH_2CN)_6(H_2O)_3]$ (**1**), $[CoFe_2O(O_2CCH_2CN)_6(H_2O)_3]$ (**2**), and $[Fe_3O(O_2CCH_2CN)_6(H_2O)_3]$-$NO_3 \cdot 5H_2O$ (**3**) at room temperature.

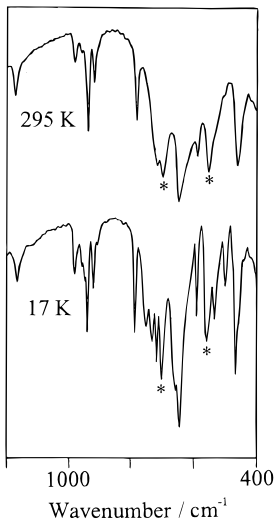

Figure 11. FT-IR spectra of a KBr pellet of $[Fe_3O(O_2CCH_2CN)_6$-$(H_2O)_3]$ (**1**) at 295 and 17 K.

IC. However, the state of the mixed-metal $CoFe_2O$ complex corresponds clearly to an orientationally (statically) disordered state denoted as phase IB below room temperature. On the other hand, the state of the mixed-valence Fe_3O complex should be a dynamically disordered state among *three* equivalent electronically localized states denoted as II above transition temperature.

Rate of Intramolecular Electron Transfer. The extra electron itinerates among the three Fe atoms at a finite rate in phase II; therefore, the mixed-valence state in phase II is largely dependent on the time scale of the observation method. By means of IR spectroscopy the mixed-valence state of **1** is determined to be trapped at any temperature below room temperature, whereas by means of ^{57}Fe Mössbauer spectroscopy it is determined to be detrapped at $T \geq 129$ K. Thus, it is concluded that the rate of electron transfer is between the ^{57}Fe Mössbauer time scale ($\sim 10^7 - 10^8$ s^{-1}) and the IR time scale ($\sim 10^{12} - 10^{13}$ s^{-1}) in the disordered phase at room temperature.

In order to quantify the valence detrapping in **1** precisely, the rate of intramolecular electron transfer has been estimated by the approach of spectral fitting for Mössbauer spectra with account taken of the relaxation effect due to intramolecular electron transfer. In the case of the present Mössbauer spectra in the high-temperature disordered phase, a typical three-site relaxation model developed by Wickman[37] is applicable because the three Fe sites are crystallographically equivalent. Since there are two equivalent Fe^{III} sites as compared to one for Fe^{II} in the localized state, the relaxation spectrum can be calculated by giving twice the weightage to Fe^{III} in the model. On the other hand, there was a problem to apply this model in the low-temperature ordered phase,[38] because the three Fe sites are not equivalent at $T < T_{trs}$. Therefore, we adopted a method for the electron exchange between inequivalent Fe sites, which requires introducing another unknown quantity p besides the relaxation time τ as follows: In the ordered phase below T_{trs}, the three interconverting localized states have different populations according to the Boltzmann distribution. The isosceles structure supports that the potential diagram consists of one deep and two equivalent or almost equivalent shallow wells, reducing the independent Fe sites to two: Fe_A and $Fe_{B,C}$. It is supposed that two minor vibronic states have equal populations; let the population be p (*vide infra*):

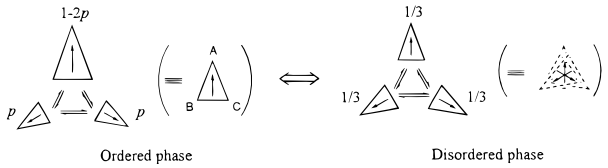

With increasing temperature, p is considered to become gradually close to $^1/_3$ and was estimated from the entropy gain at temperature T toward the total transition entropy by

$$p = \frac{1}{3}\frac{\Delta_{exc}S_m(T)}{\Delta_{trs}S_m} \quad (1)$$

The mixing of Fe^{II} and Fe^{III} at two kinds of Fe sites is represented by

$$Fe_A = (1 - 2p)Fe^{II} + 2pFe^{III} \quad (2)$$

and

$$Fe_{B,C} = pFe^{II} + (1 - p)Fe^{III} \quad (3)$$

The theoretical spectrum should be calculated for each Fe_A and $Fe_{B,C}$ site on the basis of a three-site relaxation model,[37] and the total absorption line is given by a summation of both lines.

Taking the above into consideration, the Mössbauer spectra of **1** have been computed, and the successful computer minimizations resulted in the theoretical spectra illustrated in Figure 13. The best fit values of Mössbauer parameters and the total relaxation time τ are given in Table 10. As shown in Figure 14, a least-squares fit of a straight line to an Arrhenius plot of the obtained τ yields an activation energy $E_a = 3.99$ kJ mol^{-1} = 333 cm^{-1} for the thermal electron transfer barrier in the disordered phase of **1**, although the precision is not very good because of limited available data. This value is rather smaller than the value of 470 cm^{-1} obtained by Dziobkowski et al.[36] for $[Fe_3O(O_2CCH_3)_6(H_2O)_3]$, but the latter value has been estimated on the basis of the Arrhenius plot of τ in the entire temperature region, neglecting a possible structure change, by which further revision should be required for their estimation.

(37) Wickman, H. H. In *Mössbauer Effect Methodology*; Gruverman, I. J., Ed.; Plenum: New York, 1966; Vol. 2.

(38) Although the term "ordered phase" was used here for convenience, there must be a fractional disordering of Fe_3O molecules in the low-temperature phase at temperatures where $\Delta_{exc}S_m$ is not 0, in the strict sense.

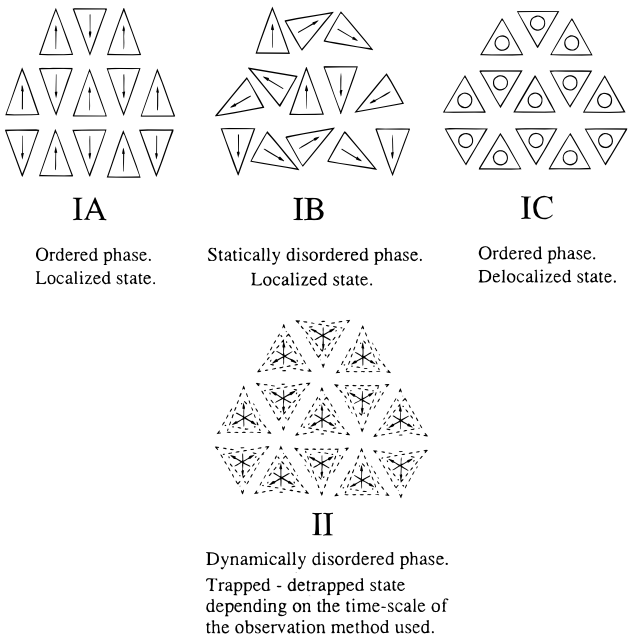

Figure 12. Four possible phases for the present trinuclear complexes. An isosceles triangle with an arrow represents a distorted M_3O unit. An equilateral triangle with a circle represents an undistorted M_3O unit. Three superimposed triangles illustrated by dashed lines represent a quickly interconverting M_3O unit.

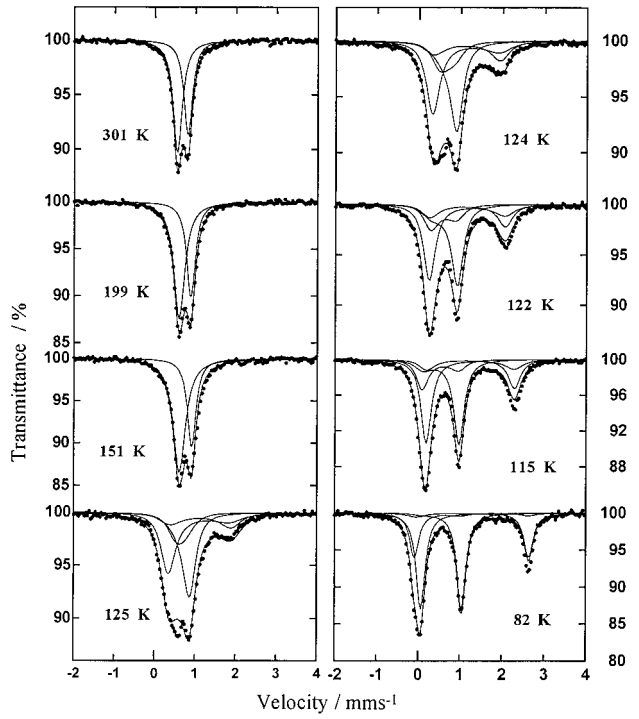

Figure 13. Mössbauer spectra of $[Fe_3O(O_2CCH_2CN)_6(H_2O)_3]$ (**1**). The solid lines represent theoretical fits obtained by the three-site relaxation model. All theoretical lines are presented.

Dziobkowski et al.[36] have pointed out that the temperature dependence of the Mössbauer spectra may be interpreted by using the PKS model.[39] Actually, the vibronic PKS model has recently been applied to available experimental data of intramolecular electron transfer in biferrocenium salts,[9,40] and it has successfully explained some aspects of their behavior, including the "fusion type" temperature dependence of Mössbauer spectra,[41] in which quadrupole-split doublets of Fe^{II} and Fe^{III} converge into one doublet without appreciable line broadening. On the other hand, no fusion type temperature dependence has ever been observed in the mixed-valence Fe_3O complexes except the solvated acetato−(4-ethylpyridine) complex, $[Fe_3O(O_2CCH_3)_6(4\text{-Et-py})_3](4\text{-Et-py})$,[7c] and most of the other Fe_3O complexes show broadened spectra at intermediate temperatures between where the spectrum shows a trapped-valence state and a detrapped-valence state. Although it is possible to fit some broadened spectra of the Fe_3O complexes by using three quadrupole doublets, Fe^{II}, Fe^{III}, and averaged-valence Fe, the fusion type cannot be completely disregarded because the broadened spectrum of Fe_3O complexes could be considered to consist of many unbroadened components which have slightly different peak positions than one another according to the distribution of the degree of fusion at an intermediate temperature. The line broadening due to the relaxation effect of intramolecular electron transfer should be confirmed by using an applicable experimental method, such as the selective

Table 10. Fitting Parameters for the Simulated Spectra on the Relaxation Model

	δ, mm s−1		ΔE_Q, mm s^{-1}			
T, K	Fe^{III}	Fe^{II}	Fe^{III}	Fe^{II}	τ, s	p
82	0.554	1.365	0.980	2.729	1.59×10^{-7}	0.0414
104	0.554	1.249	0.913	2.497	9.01×10^{-8}	0.1111
115	0.581	1.184	0.803	2.226	9.29×10^{-8}	0.1604
122	0.591	1.159	0.707	1.837	6.50×10^{-8}	0.2048
124	0.620	1.175	0.641	1.570	4.41×10^{-8}	0.2202
125	0.630	1.175	0.621	1.550	3.36×10^{-8}	0.2304

	δ, mm s^{-1}		ΔE_Q, mm s^{-1}			
T, K	Fe^{III}	Fe^{II}	Fe^{III}	Fe^{II}	τ, s	K^+, K^- [a]
151	0.503	1.291	1.076	1.241	9.71×10^{-10}	0.3500, 0.6500
198	0.486	1.260	1.082	1.304	6.29×10^{-10}	0.3889, 0.6111
251	0.461	1.205	1.069	1.336	3.73×10^{-10}	0.4200, 0.5800
301	0.434	1.170	1.058	1.340	1.84×10^{-10}	0.4387, 0.5613

[a] The proportional constants for higher-velocity peak line and lower-velocity peak line.

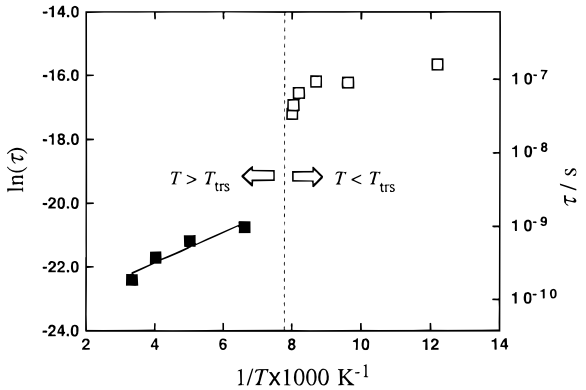

Figure 14. Plot of $\ln(\tau)$ vs T^{-1} for $[Fe_3O(O_2CCH_2CN)_6(H_2O)_3]$ (**1**). The straight line represents a least-squares fit to the data at $T > T_{trs}$.

(39) Piepho, S. B.; Krausz, E. R.; Schatz, P. N. *J. Am. Chem. Soc.* **1978**, *100*, 2996. Piepho, S. B. *J. Am. Chem. Soc.* **1988**, *110*, 6319−6326. Piepho, S. B. *J. Am. Chem. Soc.* **1990**, *112*, 4197.

(40) Sano, H. *Hyperfine Interact.* **1990**, *53*, 97 and references cited therein.

(41) Boukheddaden, K.; Linares, J.; Bousseksou, A.; Nasser, J.; Rabah, H.; Varret, F. *Chem. Phys.* **1993**, *170*, 47. Boukheddaden, K.; Linares, J.; Galam, S.; Varret, F. *J. Phys.: Condens. Matter* **1993**, *5*, 469. Boukheddaden, K.; Linares, J.; Varret, F. *Phys. Rev.* **1993**, *B47*, 14070. Boukheddaden, K.; Linares, J.; Galam, S.; Varret, F. *Chem. Phys.* **1994**, *180*, 43. Masuda et al. have beforehand succeeded in explaining the fusion type of temperature-dependent Mössbauer spectra in terms of order−disorder phase transition by assuming an Ising model: Masuda, Y.; Sano, H. *Bull. Chem. Soc. Jpn.* **1987**, *60*, 2674.

excitation double Mössbauer (SEDM) method[42] or ac-dielectric measurement, in order to improve the accuracy and precision for the rate of intramolecular electron transfer.

Mechanism of the Valence-Detrapping Phase Transition. It is known without any exceptions that the Fe_3O complexes crystallizing in a 3-fold space group exhibit a detrapped-valence state on the ^{57}Fe Mössbauer time scale at room temperature and always come to show a trapped-valence state in spite of the entropy loss when the temperature is lowered. To transform the Fe_3O molecules from the detrapped-valence state to the trapped-valence state, the system must gain stabilization energy in excess of the entropy loss. Therefore, at lower temperatures below T_{trs} there must be some lower-symmetrical environmental effects originated from an intermolecular interaction which can stabilize one of the localized vibronic states. The theoretical description based on the vibronic potential model[10,11] has also expected that one of three localized states in a mixed-valence Fe_3O molecule can become more stable microscopically in the solid state due to intermolecular interactions of neighboring molecules, while three localized vibronic states are equivalent in a free (isolated) molecule.

In the present complex, it has been ascertained by single-crystal X-ray crystallography that the symmetry of the Fe_3O molecules changes from 3-fold to a lower one as the result of the trapping of the extra electron. The electronically trapped Fe_3O molecule is expected to possess a nonzero electronic dipole moment. In the crystal of **1**, the distorted Fe_3O molecules are alternatively oriented in the opposite direction with respect to the center of symmetry, counterbalancing the whole dipole moment in the ordered phase denoted as IA in Figure 12. This suggests that the electronically localized phase can be stabilized by an intermolecular interaction in a similar way to antiferroelectric dipole−dipole interactions: Because the stabilization energy of the dipole−dipole interactions exceeds the increase of free energy due to electron trapping, the entropy loss due to the positional ordering of extra electrons and the elastic-energy gain accompanying the lattice distortion, one of the localized states comes to have the lowest energy in the solid state below T_{trs}. This phase shall be called the "antiferroelectrically ordered phase" for convenience although the actual dielectric property for the phase is not fully known. In the previous theoretical descriptions[10,43] as far as the phase transitions seen for $[Fe_3O(O_2CCH_3)_6(py)_3]py$ with the space group $R32$ is concerned, it may not be necessary to take the antiferroelectrically ordered phase into consideration, because the antiferroelectrically ordered phase can be realized as the result of lowering of a centrosymmetric space group in which a center of symmetry lies between Fe_3O molecules. The phase has never been derived from a noncentrosymmetric space group, such as $R32$, in which all of the Fe_3O triangles are oriented in the same direction. Taking into account that the valence-detrapping process is a reverse of the valence-*trapping* process, the detrapping process can be explained as follows: When the temperature is raised the contribution of the entropy term $T\Delta S$ for the free energy overcomes the antiferroelectric stabilization, and then the Fe_3O complex undergoes the phase transition from phase IA to phase II with a transition entropy of R ln 3. The intermolecular hydrogen bonds contribute little to the valence-detrapping phase transition because the transition temperature was not significantly shifted in DSC measurements by D-substitution of the water ligand of **1**.[44] Thus, there is no evidence that the intermolecular hydrogen bond induces the valence detrapping.

On the other hand, the mixed-metal $CoFe_2O$ complex shows no phase transition and no structure change, when temperature is lowered to 102 K. A similar dipole−dipole interaction is expected for **2**, but the effect may be obscured by static disorder as the $CoFe_2O$ molecules cannot crystallize in phase IA at room temperature. Therefore, both **1** and **2** crystallize in an isostructural space group $R\bar{3}$, but they show quite different thermal properties because the origin of the disordered structure is quite different. The phase transition of **1** from II to IA occurs as the extra electrons cease to itinerate, whereas the phase transition of **2** from IB to IA requires an atomic positional change between Fe and Co sites or the rearrangement of the randomly oriented $CoFe_2O$ molecules in the crystal. Both of the conditions for **2** are considered to be almost impossible because a very large activation energy will be required, even if phase IA were more stable than phase IB at low temperatures. If **2** could be recrystallized at very low temperature, it may crystallize in phase IA and may not undergo a phase transition from IA to IB on raising the temperature with the same reason as for the impossibility of the phase transition from IB to IA.

Summary

In the present study on the mixed-valence complex $[Fe_3O(O_2CCH_2CN)_6(H_2O)_3]$ (**1**), precise information on the valence-detrapping phase transition was obtained and the mechanism of the phase transition was discussed.

Since **1** exhibits a first-order phase transition, it is evident that an intermolecular interaction plays an important role in the cooperative valence-detrapping phenomenon of **1**. The transition entropy was estimated to be about R ln 3 in this complex as the first case where the transition entropy includes only the contribution from the valence detrapping. Although the contribution of the statically *delocalized* state in the dynamically disordered phase has been suggested for $[Fe_3O(O_2CCH_3)_6(py)_3]\cdot CHCl_3$[8c] and $[Mn_3O(O_2CCH_3)_6(py)_3]py$[45] in order to explain their transition entropies, their transition entropies are quite large, $\sim R$ ln 32 and $\sim R$ ln 72, respectively, because of the orientational disorder of solvate molecules. The contribution of the statically delocalized state would be confirmed empirically by an investigation for nonsolvated complexes which show a neat valence-detrapping phase transition only due to the intramolecular electron transfer. It should be pointed out here that Cannon et al. have recently proposed a possible electron transfer between only two Fe atoms in the structurally similar complex $[Fe_3O(O_2CCMe_3)_6(py)_3]$.[46]

The lowering of the molecular symmetry accompanied by the electron trapping has been confirmed by single-crystal X-ray crystallography for the first time, and in the low-temperature ordered phase, the distorted Fe_3O molecules are found to be alternatively oriented in an opposite direction as if they are oriented by antiferroelectric intermolecular interaction. It is likely that the most important intermolecular interaction to turn on or off the intramolecular electron transfer in this complex crystal is an antiferroelectric dipole−dipole intermolecular interaction.

The mechanism proposed here for the valence-detrapping phase transition has been derived only from the information on

(42) Balko, B.; Hoy, G. R. *Phys. Rev.* **1974**, *B10*, 36.
(43) Stratt, R. M.; Adachi, S. H. *J. Chem. Phys.* **1987**, *86*, 7156. Adachi, S. H.; Panson, A. E.; Stratt, R. M. *J. Chem. Phys.* **1988**, *88*, 1134.
(44) Unpublished.
(45) Nakano, M.; Sorai, M.; Vincent, J. B.; Christou, G.; Jang, H. G.; Hendrickson, D. N. *Inorg. Chem.* **1989**, *28*, 4608.
(46) Wu, R.; arapKoske, S. K.; White, R. P.; Anson, C. E.; Jayasooriya, U. A.; Cannon, R. D. *J. Chem. Soc., Chem. Commun.* **1994**, 1657.

1. Crystal structure information of the other complexes in the low-temperature ordered phase is necessary for further clarification of the valence-detrapping phenomenon in the Fe_3O type complexes.

Acknowledgment. We wish to thank Prof. Haruo Sato (deceased) of Science University of Tokyo for his kind manufacturing of a sample holder and variable-temperature IR measurements. We also thank Prof. Isao Ikemoto, Prof. Koichi Kikuchi of Tokyo Metropolitan University, and Dr. Hideki Saito of Saitama University for their help for X-ray structure determinations. Thanks are given to Dr. Atsushi Kubo of Kyoto University for his guidance for the interpretation in terms of electronic relaxation.

Supporting Information Available: Tables listing detailed crystallographic data, atomic positional parameters including H atoms, anisotropic thermal parameters (*U*'s) for non-H atoms, bond lengths and angles, torsion angles, least-squares planes, and molar heat capacities for **1** and **2** and figures illustrating complete Mössbauer spectra and recoilless fraction for **1** and IR data, XRD pattern, DSC thermogram, and Mössbauer spectra for partly deuterated **1** (38 pages). Ordering information is given on any current masthead page.

IC961438W